Dynamics of proton transfer from ArH+ to CO

Björn Bastian[a], Eduardo Carrascosa[a,1], Alexander Kaiser[a], Jennifer Meyer[a], Tim Michaelsen[a], Gábor Czakó[b], William L. Hase[c], Roland Wester[a,*]

[a] Institut für Ionenphysik und Angewandte Physik, Universität Innsbruck, Technikerstraße 25/3, 6020 Innsbruck, Austria
[b] Interdisciplinary Excellence Centre and Department of Physical Chemistry and Materials Science, Institute of Chemistry, University of Szeged, Rerrich Béla tér 1, Szeged H-6720, Hungary
[c] Department of Chemistry and Biochemistry, Texas Tech University, Lubbock, TX 79409, United States

ARTICLE INFO

ABSTRACT

The reaction of ArH+ with CO is a fast proton transfer reaction that can form two different isomers, HCO+ and HOC+. It has been investigated in a crossed beam experiment and with direct dynamics simulations at collision energies ranging from 0.4 to 2.4 eV. Images of the differential cross sections reveal dominant forward scattering, which is evidence for direct dynamics. The measured product internal energies are primarily determined by the reaction enthalpy and only at large scattering angles depend noticeably on the collision energy. The computational results agree well with the measured internal energy and scattering angle distributions and with the previously measured total rate constant. The direct reaction dynamics with dominant forward scattering are well reproduced by the almost step like opacity functions. The HCO+/HOC+ branching is found to be close to 2:1 in the simulations at 0.83 eV and 2.37 eV collision energy. A mode-specific vibrational analysis provides further insight into the isomer specific distribution of the product internal excitation.

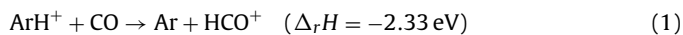© 2018 Elsevier B.V. All rights reserved.

1. Introduction

Ion-molecule reactions, often near the collision rate, compete with neutral reactions at low temperatures [1]. They are therefore important to understand the composition and observed abundances of molecules in cold planetary or interstellar gas clouds. Proton transfer is a prominent mechanism that is known to proceed rapidly in exothermic reactions [2]. A rich network of ion-neutral reactions in the interstellar medium is initiated by proton transfer reactions of H_3^+ which has a lower proton affinity than most interstellar atoms and molecules [3,4]. Among them is CO, the precursor for the formyl cation HCO+ that in many cases is the most abundant molecular ion [5]. Also the metastable isoformyl cation HOC+ is formed in this reaction and has been observed in dense molecular clouds [6,7]. The HCO+/HOC+ branching ratio in different environments and future detections are subject to ongoing interest [8–11] and comparison to models suggests that HOC+ must be considered in reliable abundance calculations [12]. Also the rapid HOC+

to HCO+ conversion by H_2 was subject to a controversial discussion [9,13].

The product branching of the most important formation pathway H_3^+ + CO is not yet fully clarified [12,14]. Investigation of the simpler four atom system ArH+ + CO can contribute to understand the general characteristics of proton transfer reactions that produce different isomers. ArH+ has been identified in the Crab Nebula in 2013 as the first noble gas compound detected in space [15]. Further detections in different galactic and extragalactic sources followed in 2015 [16,17]. Argonium is a good tracer of the almost purely atomic, diffuse interstellar medium with a low fractional H_2/H abundance in the 10^{-4}–10^{-3} range [16,17]. Isotopic ^{36}Ar/^{38}Ar ratios are significantly lower than the solar value and future observations of isotopic ratios with redshift may provide useful constraints for nucleosynthesis models [17].
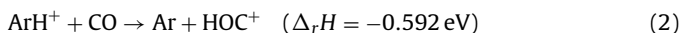
Interstellar ArH+ is formed via ionisation of atomic argon by cosmic rays followed by the reaction with molecular H_2, and is mainly destroyed by photodissociation or proton transfer to neutral molecular hydrogen or atomic oxygen [16]. Chemical models of the Martian atmosphere also include fast proton transfer from argonium to several other neutrals [18,19]. The proton transfer reaction

$$ArH^+ + CO \rightarrow Ar + HCO^+ \quad (\Delta_r H = -2.33\,\text{eV}) \tag{1}$$

$$ArH^+ + CO \rightarrow Ar + HOC^+ \quad (\Delta_r H = -0.592 \, eV) \quad (2)$$

is exothermic for both the formyl and isoformyl cation. The reaction enthalpies $\Delta_r H$ are derived from the proton affinities of the neutral species [20–24]. The total rate coefficient for $ArH^+ + CO$ is $1.25(35) \times 10^{-9} \, cm^3 \, s^{-1}$. It has been measured in a drift tube from the thermal range to about 2 eV and is nearly independent of the kinetic center-of-mass energy which is typical also for other exothermic proton transfer reactions [25]. The capture rate $k_c = 8 \times 10^{-10} \, cm^3 \, s^{-1}$ is smaller than the reported value but within two standard deviations of the experimental result. While recent models [18,19] assume HCO^+ as the only product, experimental or theoretical evidence for the product partitioning into HCO^+ and HOC^+ is still missing [26].

Here we present a combined experimental and computational investigation of the title reaction in the 0.4–2.3 eV energy range. These studies extend experimental insight into the title reaction to reaction dynamics and product branching. With its focus on the HCO^+/HOC^+ ratio, this work is in line with previous crossed beam experiments on the proton transfer reaction of the important interstellar molecules H_3^+ and $HOCO^+$ with CO [14,27].

2. Methods

2.1. Crossed beam imaging

Angle- and energy differential cross sections of the title reaction have been recorded in a crossed beam imaging setup at four different collision energies from 0.4 to 2.4 eV. We refer to previous publications for a detailed description of the setup [28,29]. As a precursor, argon was ionised in a plasma discharge and trapped in a radio frequency octupole ion trap for thermalisation at room temperature. Molecular hydrogen was admixed to the argon buffer gas in the trap (20% H_2 in Ar) to react exothermically with Ar^+ to form ArH^+ ($\Delta H = -1.5 \, eV$ [30]). In 10 ms, an ArH^+/Ar^+ ratio of about 2:1 was achieved and after 40 ms trapping time, no residual Ar^+ could be detected. The extracted ArH^+ beam was crossed with a neutral CO beam formed in a supersonic expansion (20% CO in Ar). The charged products were then mapped on a position and time sensitive detector with the velocity map imaging technique [31,32]. For each event, the three-dimensional product velocity is reconstructed in the center-of-mass frame of the collision. Velocity distributions are binned with respect to the velocity components parallel (v_x) and perpendicular (v_r) to the collision axis and weighted by the inverse perpendicular velocity. The resulting images correspond to slice distributions of reactive scattering that are comparable to other experiments. Alternately, 1000 foreground and 100 background loops were recorded in order to subtract events that are not related to reactive collisions. For the background measurements, the neutral beam was pulsed at a later time to avoid crossing with the ion beam, while maintaining the total pressure in the scattering chamber. N_2 contamination or CO that diffuses from the scattering chamber to the trap may form N_2H^+ or HCO^+/HOC^+ background ions with the same nominal masses. They interfere with the large angle region of the scattering images at the two largest collision energies.

Velocity map imaging is also used to characterise the reactant ion and neutral beams for which the latter is ionised by electron impact. The experiments were performed at ion energies from 1 to 6.4 eV with a standard deviation ranging from 70 to 110 meV. The mean kinetic energy of the neutral beam was 117 meV with a fitted standard deviation of 20 meV that corresponds to a translational temperature of 13 K. Convolution of both velocity distributions determines the mean collision energies and upper limits for their spread (Gaussian standard deviation), that is 0.38(2) eV, 0.83(4) eV, 1.59(4) eV and 2.36(5) eV. The beams were crossed at an angle of 68°
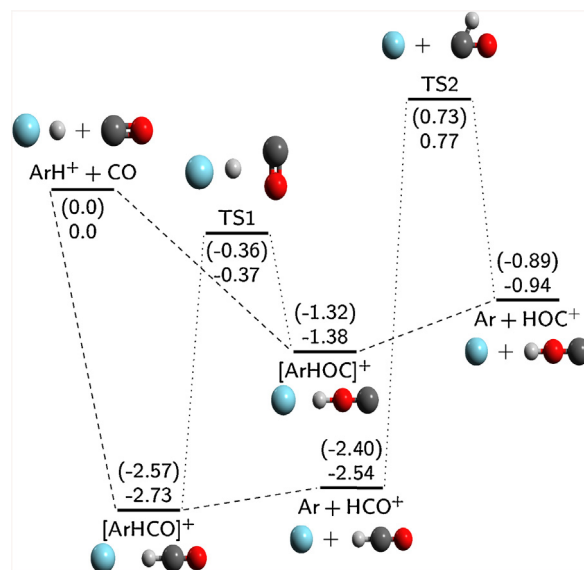

Fig. 1. Schematic energy profile for the proton transfer from ArH^+ to CO. The PBE0 energies using the 6-31G(d,p) basis set are given in eV relative to the reactants. Values in brackets include zero-point energies. The zero-point energy for the reactants amounts to 0.31 eV. TS1 and TS2 are the transition states of the argon catalysed and free HCO^+/HOC^+ isomerisation.

with angle spreads of 2.4° for the neutral beam and less than 0.5° (1° at the lowest energy) for the ion beam. The resulting energy and angular resolution in the center-of-mass frame was estimated as described previously [28]. The standard deviations from Gaussian error propagation are not larger than 90 meV for the center-of-mass kinetic energy and 2.1° (3.3° at the lowest energy) for the scattering angle.

2.2. Quasiclassical trajectory simulations

Direct dynamics simulations of the title reactions were performed with VENUS/NWChem [33–35] at 0.83 eV and 2.37 eV collision energy. The trajectories were integrated by the Velocity Verlet algorithm using a 0.2 fs timestep with on-the-fly calculations of the forces. All electronic structure calculations used density functional theory (DFT) with the PBE0 hybrid density functional [36] and 6-31G(d,p) basis set [37]. This rather small basis set was chosen for computational efficiency of the trajectory simulations. Stationary point and zero-point energies for the reactant system, product channels, intermediates and transition states are given in Fig. 1. Going to the larger triple-zeta 6-311G(d,p) basis set changes the stationary energies by typically +0.1 eV and +0.2 eV for the $Ar + HOC^+$ asymptote. The smaller basis set reproduces the experimental exothermicities in Eqs. (1) and (2), derived from the proton affinities of the neutral species, up to deviations of 0.07 eV and 0.3 eV with the PBE0 functional. The computed CO proton affinity at the carbon end of 6.16 eV coincides with the literature value [20]. The value obtained at the oxygen end is 0.23 eV larger (4.56 eV) than the published value of 4.42 eV [20].

Initial conditions for rotation and vibration were chosen from the rotating Morse oscillator model and sampled from a temperature of 13 K for CO and 295 K for ArH^+ to resemble the experimental conditions. Fits to DFT points for CO and ArH^+ dissociation determined the parameters of the Morse potentials ($D_e = 15.7/3.76 \, eV$, $\beta = 2.12/1.99 \, Å^{-1}$ and $r_0 = 1.14/1.29 \, Å$ for CO/ArH^+). The impact parameter b was sampled from a homogeneous distribution within a circular disc with radius $b_{max} = 6.5 \, Å$. The homogeneous sampling was insufficient to calculate reliable reaction probabilities for

$b < 0.9$ Å. Only for this purpose, 216 and 220 additional trajectories were computed for the two collision energies. The diatomic reactants were initially separated by 10 Å along the collision axis plus the perpendicular separation b, that is $(10^2 + b^2)^{0.5}$ Å. Products were generally identified at 11 Å separation by distance criteria.

For the mode-specific vibrational analysis of the charged products, we calculated the harmonic normal modes of the equilibrium structures of HCO^+ and HOC^+ with the same level of theory. Each product molecule at each timestep was rotated using the Eckart transformation [38–40]. After this operation, the product molecule has a similar orientation compared to the equilibrium structure and displacements of atoms from its equilibrium positions become minimal. The Eckart transformed velocities and displacements were then transformed again using the transformation matrix between Cartesian and normal mode coordinates from the harmonic frequency analysis. These coordinates and velocities yield mode-specific vibrational energies in the harmonic approximation as described in more detail in [40]. In geometries far from the equilibrium structure, the harmonic potential energy may largely deviate from the true potential energy of the analyzed product relative to its equilibrium potential energy. To suppress unphysically large harmonic actions, it was suggested to extract the geometry with the minimum potential energy from the last vibrational period [41]. In a similar way, we applied the analysis to the final product in the last fifty timesteps of each trajectory and filtered out all timesteps, for which the total harmonic potential energy deviates more than 0.2 eV from the correct calculated potential energy. With this approach, accurate mode energies were obtained by primarily using the kinetic energy.

3. Results and discussion

3.1. Experimental results

Differential cross sections of the proton transfer reaction of ArH^+ with CO have been measured at four different collision energies 0.38(2) eV, 0.83(4) eV, 1.59(4) eV and 2.36(5) eV. The product ion velocity distributions are presented in Fig. 2 together with the distributions of the relative kinetic energy before the collision (orange, denoted as the collision energy) and after collision (blue) and the derived energy of internal excitation of the products (black).

At all energies, the proton transfer dominantly proceeds in forward direction of the product ion relative to the neutral reactant with small angular deflection. The forward directionality is more pronounced at higher collision energies, see Fig. 3a. Large noise from the background subtraction at about 180° backward scattering at the two highest collision energies is due to background ions.

The amount of energy attributed to the rovibrational excitation (internal energy) of the products can be calculated from the product ion velocities by means of momentum and energy conservation. The total available center-of-mass energy is the sum of the collision energy and reaction exothermicity (disregarding initial thermal excitation of ArH^+) and referred to as the kinematic cutoff. It corresponds to products in their ground state and is marked by the outermost black and red circles for the HCO^+ and HOC^+ products in Fig. 2 (middle panel). The interior rings indicate energy differences to the cutoff in steps of 1 eV. Because the neutral product is a rare gas atom, the differences can be fully attributed to internal excitation of the charged products. The kinematic cutoff and
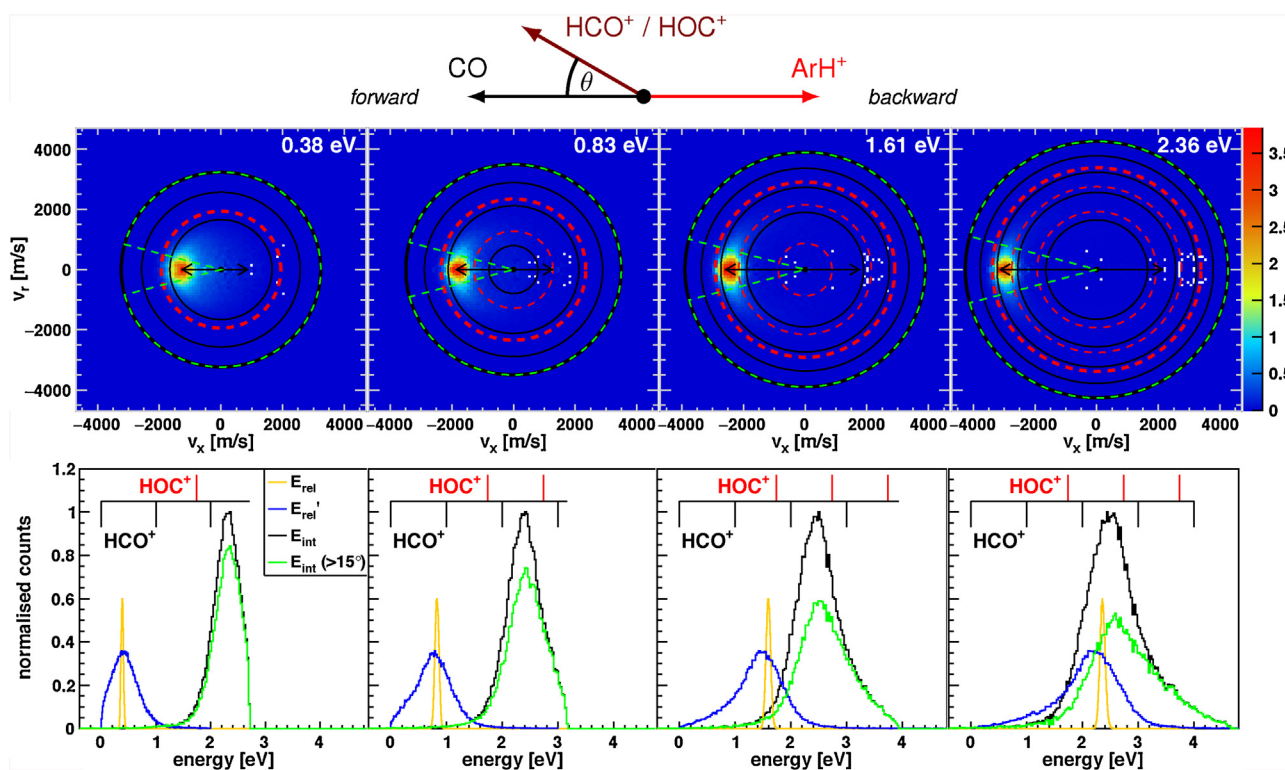

Fig. 2. Product ion velocity and internal energy distributions of the proton transfer reaction $ArH^+ + CO$ at four different collision energies. *Upper panel*: Newton diagram of the collision in center-of-mass frame illustrating the orientation and scattering angle θ. *Middle panel*: Experimental product ion velocity distribution. The Newton rings correspond to the kinematic cutoff for HCO^+ (black)/HOC^+ (red dashed) and 1 eV spacings. *Lower panel*: Internal energy distributions (black) with the Newton ring energies as inset axis. Large angle scattering ($\theta > 15°$) distributions are shown in green for the cuts depicted by dashed green lines in the velocity images. Additionally, the relative kinetic energies before (orange) and after (blue) the collision are shown. (For interpretation of the references to color in this figure legend, the reader is referred to the web version of this article.)
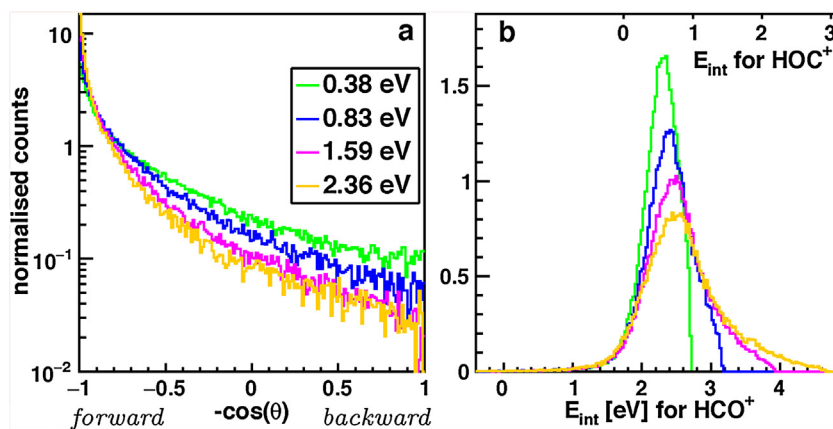
Fig. 3. Collision energy dependence of scattering angles and product excitation. (a) Distributions of the cosine of the scattering angle. The noise at large angles is due to background ions. (b) Internal energy distributions with two axes relative to the HCO$^+$ and HOC$^+$ ground states.

1 eV spacings are also shown by the black and red inset axes in the internal energy distributions in the lower panel of Fig. 2. At all collision energies, the distributions rise near the kinematic cutoff of the HOC$^+$ product and extend as far as the available energy allows. Unexpectedly, the difference in exothermicity does not let us discriminate the reaction channels (1) and (2): the reactive collisions may either be attributed to HCO$^+$ products with internal excitation above 2 eV or to HOC$^+$ products with smaller internal excitation. In other words, it is not observed that the additional exothermicity that is available for HCO$^+$ compared to HOC$^+$ is converted into relative kinetic energy. Instead, this additional exothermicity leads to higher internal excitation.

Overall, the collision energy essentially determines the average relative kinetic energy of the products (see Fig. 2, lower panel), while the maxima of the internal excitation are close to the reaction exothermicity at 2.33 eV for HCO$^+$ (0.59 eV for HOC$^+$) as is seen best in Fig. 3b. Energy transfer between collision and internal energy and between exothermicity and relative kinetic energy of the products seems to be small. In contrast to the small shift of the mean internal excitation with the collision energy, the full distribution is relatively narrow and symmetric at 0.38 eV but broadens strongly towards higher excitation when the collision energy is increased. To differentiate these two features, it is instructive to consider the distributions restricted to angular deflections *larger* than 15° in the lower panel of Fig. 2 (green lines), where it is seen that the large angle scattering accounts for the major part of the broadening at higher collision energies. The same can be seen directly with small and large angle cuts applied to the internal energy distributions in Fig. 4a. The 0–5° sliced distribution shifts only slightly with increasing collision energy while the 55–65° distribution lies at significantly higher energies as far as the total available energy allows.

To quantify this behaviour, the mean internal energy was calculated for the ±5° slice distributions from 0 to 110° in steps of 10° and is presented for all collision energies in Fig. 4b. Small angle scattering is characterised by a mean product internal energy close to the reaction exothermicity almost independently of the collision energy. This is equivalent to similar initial and final kinetic energies. The transfer of collision energy into internal excitation becomes important only for larger scattering angles. At angles above 50°, a substantial amount of kinetic energy is converted into internal energy. In order to quantify the latter by a relative measure, we consider the fraction f_{int} of the internal energy relative to the total available energy in Fig. 4c. While the internal energy at small scattering angles is always close to the exothermicity, the internal energy *fraction* for different collision energies approaches similar values in the 74 to 87% range at large scattering angles. While the

energy scales in Fig. 4 assume the exothermicity for formation of HCO$^+$, the same graphs for the HOC$^+$ channel look very similar; i.e. the difference of the exothermicities leads to a shift of the E_{int} axis. The f_{int} axis is shifted and rescaled as a function of the collision energy.

The findings described above are in strong contrast to the proton transfer from HOCO$^+$ + CO that were investigated at energies ranging from 0.3 to 2.3 eV in a previous publication [27]. In this case, the formation of HOC$^+$ is endothermic by 1.18 eV and the internal energy distributions rise at the kinematic cutoff for the exothermic formation of HCO$^+$ ($\Delta_r H = -0.55$ eV). Up to the highest collision energy, the major part of the internal energy distribution is located below the HOC$^+$ formation threshold. The HOC$^+$ product is only accessible in the high energy range that is, similarly to the results presented here for ArH$^+$, dominated by large angle scattering. The ArH$^+$ + CO system with little exchange between kinetic and internal energy features similar internal energies for both isomeric products with respect to the HCO$^+$ ground state. On the other hand, the formation of HOC$^+$ from HOCO$^+$ requires the transfer of a substantial amount of the collision energy into potential energy. Assuming, for both isomers, identical fractions of the internal energy relative to the total available energy for the respective isomer—a reasonable approach for the reaction with HOCO$^+$ but not for the reaction with ArH$^+$—an upper limit of <2% for the HOC$^+$ fraction was obtained from a two-isomer fit in [27].

Another reaction for which the formation of both product isomers is exothermic, is the proton transfer from H$_3^+$ to CO ($\Delta_r H = -1.76/-0.13$ eV). Previous crossed beam experiments [14] in the 0.2 to 4.3 eV collision energy range reveal monomodal internal distributions as in the reactions with HOCO$^+$ and ArH$^+$. Substantial parts of the distribution reside below the kinematic threshold of HOC$^+$ formation but at 1.8 eV collision energy and above, the dominant part allows for both isomers and ranges into the autoisomerisation domain at higher energies. In this respect, we may regard the H$_3^+$ + CO reaction as an intermediate case which is also justified by the reaction enthalpy between the more and less exothermic reactions with ArH$^+$ and HOCO$^+$.

Given the measured internal energy distributions, we gain no direct insight into the product branching of the ArH$^+$ + CO reaction from the experimental data alone. To correctly disentangle the two reaction channels, we therefore use direct dynamics simulations.

3.2. Simulation results

Direct dynamics simulations have been performed for the ArH$^+$ + CO system at collision energies of 0.83 eV and 2.37 eV. For each energy, more than 5500 trajectories were started with impact
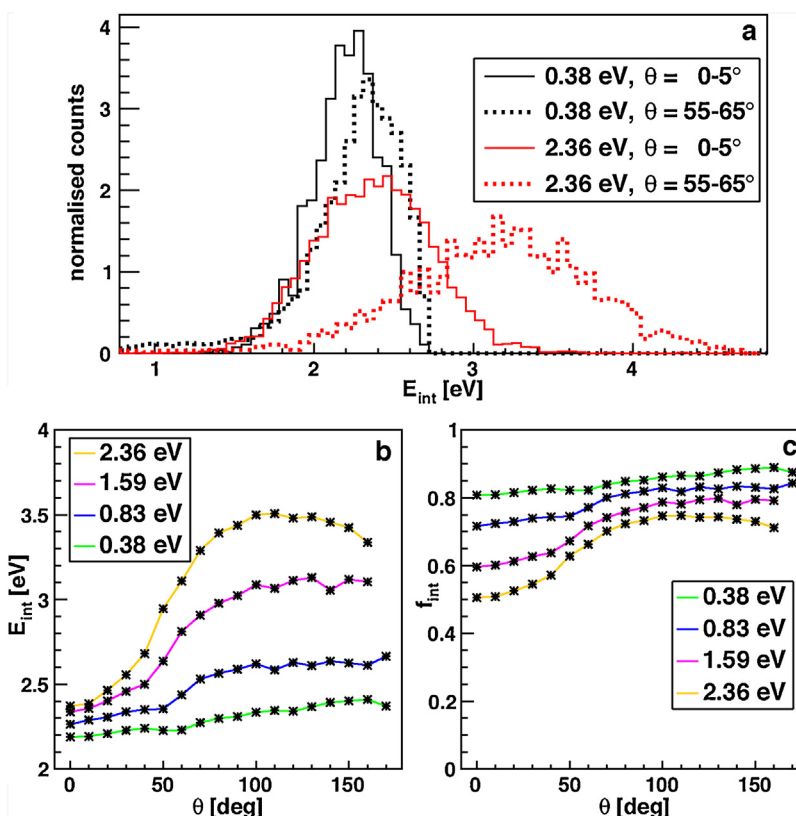
Fig. 4. Angle-differential mean internal energies. Energies are shown relative to the HCO⁺ ground state. (a) Scattering angle slices $\theta = 0$–$5°$ and 55–$65°$ for two collision energies. (b) Mean internal energy and (c) fraction of the mean internal energy relative to the total available energy as a function of the scattering angle for four collision energies. The largest angles at the two highest collision energies were dominated by background ions and omitted.

Table 1
Total number of simulations, total and product specific number of reactive trajectories and the maximum impact parameter for simulations at two collision energies.

Energy	b_{max}	Total	Reactive	HCO⁺	HOC⁺
0.83 eV	6.5 Å	5607	1740	1159	581
2.37 eV	6.5 Å	5982	1097	724	373

Table 2
Simulated reactive cross sections and rate constants. The initial collision energies and relative velocities are given in the first two columns. From the reaction probability p_r and maximum initial impact parameter b_{max}, the reactive cross section σ_r and rate constant k were calculated as $\sigma_r = p_r \pi b_{max}^2$ and $k = v_{rel}\sigma_r$.

Energy	v_{rel} [m/s]	p_r	σ_r [Å²]	k [cm³ s⁻¹]
0.83 eV	3133	31.0%	41.2	1.29×10^{-9}
2.37 eV	5244	18.3%	24.3	1.28×10^{-9}

parameters b within a circular disc with $b < b_{max} = 6.5$ Å. The homogeneous sampling within the disc is confirmed by the histogram of the sampled impact parameters b in Fig. 6 (gray points with a linear fit). Table 1 summarises the number of simulated and reactive trajectories. With the ratio p_r of the reactive to total number of trajectories and the relative velocity of the reactants v_{rel} we obtain the reactive cross section σ_r and reaction rate $k = 1.29 \times 10^{-9}$ cm³ s⁻¹ (1.28×10^{-9} cm³ s⁻¹ at 2.37 eV collision energy) in Table 2.

The reaction rate only negligibly depends on the collision energy and compares well with the experimental value $1.25(35) \times 10^{-9}$ cm³ s⁻¹ by Villinger et al. [25] Both are larger than the capture theory rate $k_c = 8.0 \times 10^{-10}$ cm³ s⁻¹ calculated from the mean polarizability $\bar{\alpha} = 13.08 a_0^3$ of CO reported by Diercksen et al. [42] This is reflected by the reactive cross sections of 41.2 and

24.8 Å² that are larger than the capture cross sections of 25.8 and 15.3 Å², respectively at 0.83 and 2.37 eV collision energy.

We obtain the HCO⁺/HOC⁺ product branching ratio of about 2:1 from Table 1 (1.99:1 and 1.94:1 at 0.83 and 2.37 eV, respectively). The analysis of the reaction probability as a function of the initial orientation of the bimolecular reactants with respect to their relative velocity reveals that the ArH⁺ orientation only slightly influences the total reactivity. The CO orientation has a strong effect on the outcome of a single reaction (see Fig. 5). At 0.83 eV collision energy, only HOC⁺ is formed if the *oxygen* atom is oriented towards ArH⁺ up to an angle of 45° with respect to the relative velocity. The probability of HCO⁺ then rises linearly with larger angles and the opposite is true if the *carbon* atom is oriented towards ArH⁺. The linear dependence is also seen at 2.37 eV collision energy but without the pronounced threshold behaviour.

We now give a comparison to the experimental data and then go more into detail on the simulation results. The statistics of the direct dynamics simulations are inadequate for a direct comparison to the measured two-dimensional differential cross sections. Instead, we compare the well sampled one-dimensional angle and internal energy distributions.

The measured and simulated scattering angle distributions in Fig. 7 compare well on a logarithmic scale up to large scattering angles. The measured distribution drops faster at angles near and above 90° especially at the higher collision energy. The simulations do not reveal striking differences between the two product channels given the small number of reactive trajectories for large scattering angles.

The calculation of the internal energy using the reaction exothermicity depends on the final products. Because the isomers cannot be separated in the crossed beam experiment, we refer to the internal energy E_{int} relative to the HCO⁺ ground state. It
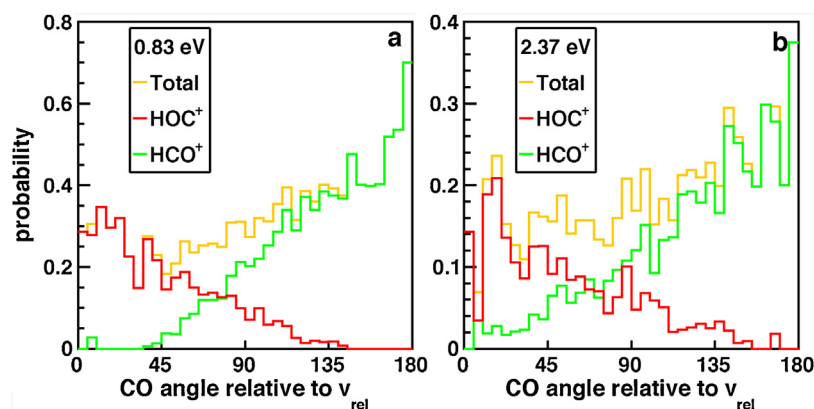
Fig. 5. Reaction probability as a function of the initial CO orientation angle with respect to the relative velocity v_{rel} of the reactants. An angle of $0°$ corresponds to the oxygen atom being aligned towards the ArH$^+$ reactant ion.
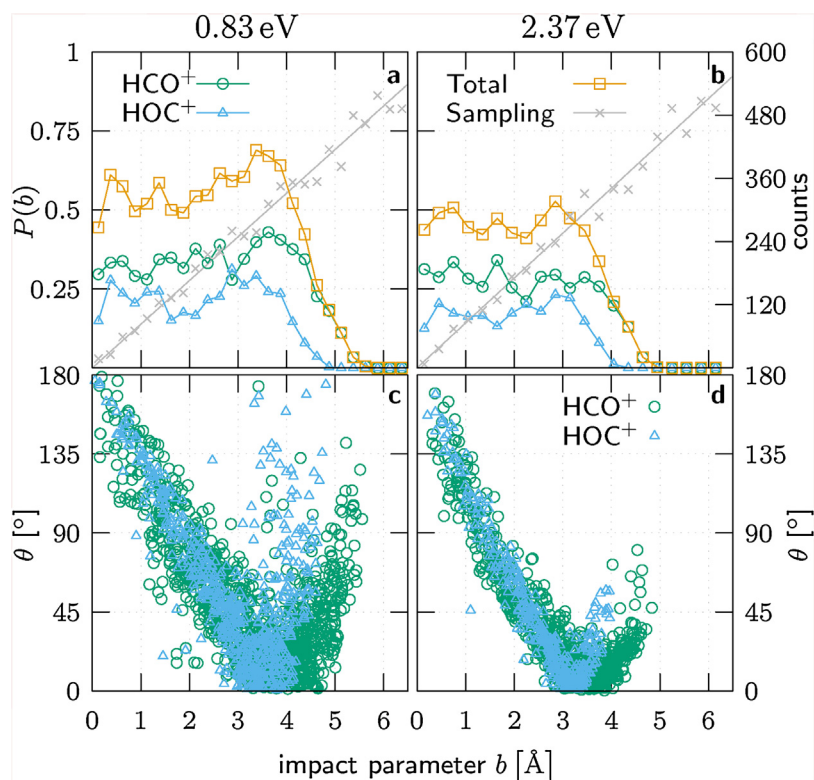

Fig. 6. Simulated opacity function $P(b)$ and scattering angles as a function of the impact parameter b. The total reaction probability and the separate HCO$^+$ and HOC$^+$ contributions are shown for (a) 0.83 eV and (b) 2.37 eV collision energy. The number of simulated trajectories in each interval is given by the alternate y-axis. Scattering angles at (c) 0.83 eV and (d) 2.37 eV collision energy are distinguished for the two reaction channels by different symbols.
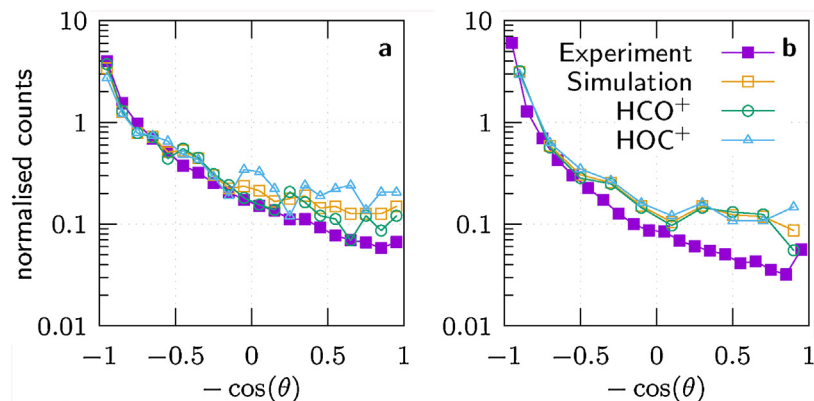

Fig. 7. Scattering angle distributions from experiments and simulations at (a) 0.83 eV and (b) 2.37 eV collision energy. Separate distributions of the simulated products are shown as well.
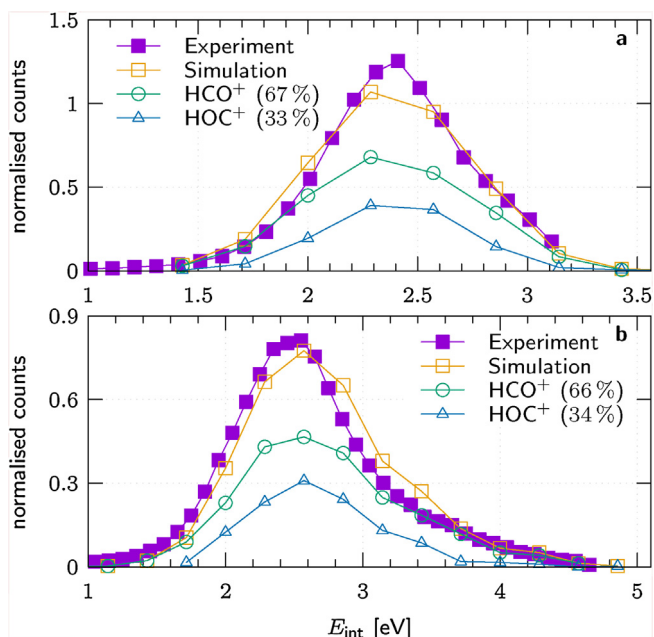
Fig. 8. Distribution of the product internal energy at (a) 0.83 eV and (b) 2.37 eV collision energy. The total distribution from the direct dynamics simulations (orange squares) is the sum of the distributions of the products (green circles and blue triangles) and is normalised to a total area of one. The internal energy for both HOC⁺ and HCO⁺ is given relative to the HCO⁺ ground state. (For interpretation of the references to color in this figure legend, the reader is referred to the web version of this article.)

includes both rovibrational excitation and isomerisation energy when related to the HOC⁺ products, which are clearly distinguished in the simulations. As opposed to the approximate internal energy derived from experimental data, the simulation results additionally include the small and almost negligible initial excitation of the reactants. The simulated total E_{int} distributions match closely to the measured distributions at both simulated collision energies in Fig. 8. At 0.38 eV collision energy, the total E_{int} distribution separates into 67% of the HCO⁺ and 33% of the HOC⁺ product with very similar mean and spread, 2.4 ± 0.4 and 2.4 ± 0.3 eV. This explains the absence of a clear indicator for a second product channel in the experimental data. Similarly, HCO⁺ and HOC⁺ contribute 66% and 34% to the reactivity at 2.37 eV with mean and spread 2.7 ± 0.6 and 2.7 ± 0.5 eV.

Two idealised model cases of distributing the available energy for the two isomers are (a) similar kinetic energy distributions and (b) similar fractions f_{int} of the internal energy relative to the available energy (relative energy losses). For comparison with our experimental data, we calculate $f_{int} = \langle E_{int} \rangle / E_{max}$. Neglecting initial excitation of the reactants, $E_{max} = E_{rel} + E_{exo}$ and $\langle E_{int} \rangle = E_{max} - \langle E'_{rel} \rangle$, with the collision energy E_{rel}, zero-point corrected exothermicities E_{exo} from Fig. 1 and the relative energy after collision E'_{rel}. In the present work, we found a situation that corresponds to case (a) with similar kinetic energy distributions for the two isomers. The obtained relative energy losses for HCO⁺/HOC⁺ are $0.72 \pm 0.11 / 0.49 \pm 0.17$ and $0.56 \pm 0.13 / 0.35 \pm 0.15$ at 0.83 eV and 2.37 eV collision energy.

In contrast to the present reaction system, the previously studied reaction of HOCO⁺ + CO is incompatible with case (a), because almost all products have kinetic energies above the kinematic cutoff for the formation of HOC⁺ [27]. Instead, case (b) has been assumed to estimate an upper bound of the HOC⁺ fraction. The same model was used for the H₃⁺ + CO reaction to derive upper bounds of 24% at 1.8 eV and 10% at lower collision energies [14]. In light of the present results for ArH⁺, it becomes apparent that energy distributions corresponding more to the case (a) can actually not be excluded for the reaction of H₃⁺. This would yield larger HOC⁺ fractions for the reaction of H₃⁺ + CO than previously estimated. Such larger HOC⁺ fractions are supported by recent chemical dynamics simulations [43], even though the simulated internal energy distributions do not quantitatively agree with the experiments.

Angle dependent product internal energies with their standard deviations in 10° slices are presented in Fig. 9. There is good agreement with the experimental results up to 60–90°. Despite large statistical fluctuations at the larger collision energy, there is a clear trend for larger internal excitation at larger angles but the mean internal energy is slightly underestimated by the simulations mainly due to the HOC⁺ products. This seems surprising given the theoretical zero-point corrected exothermicity of 0.89 eV that is larger than the experimental value of 0.6 eV. More significant is the separation of the mean internal energies (always relative to the HCO⁺ ground state) of the different products at large angles especially at 2.37 eV collision energy. The inefficient transfer of kinetic into internal energy, measured for low scattering angles and small energies, suggests an influence from the different exothermicities predominantly at larger scattering angles.

More insight into the dynamics of the title reaction is gained from the opacity functions, which are presented in Fig. 6. The reaction probabilities are coarsely constant between 0.6 (lower energy) and 0.5 (higher energy) on a range of impact parameters well beyond the capture limits of 2.86 and 2.20 Å. The thermodynamically favoured HCO⁺ is the more likely and at large impact parameters (>4 Å at 2.37 eV) only product. This is understood by the dipole moment of C–O⁺ in the order of 0.12 debyes [42] that favours the orientation of the C side towards ArH⁺. Since larger impact
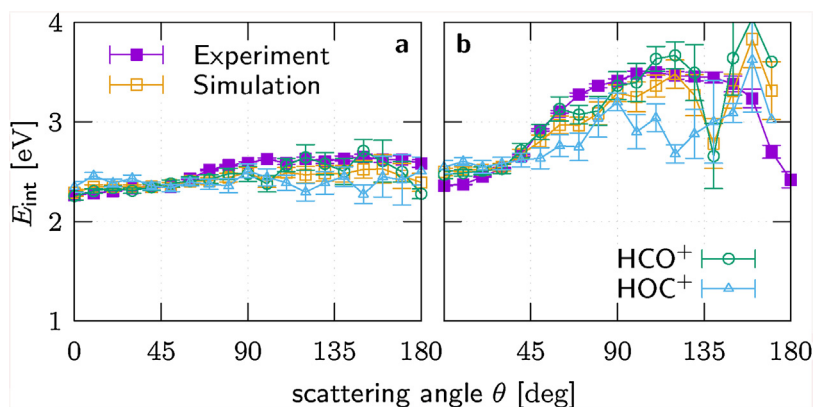

Fig. 9. Experimental and simulated angle-differential mean internal energies at (a) 0.83 eV and (b) 2.37 eV collision energy. Simulated results for HCO⁺ and HOC⁺ products are also shown separately.
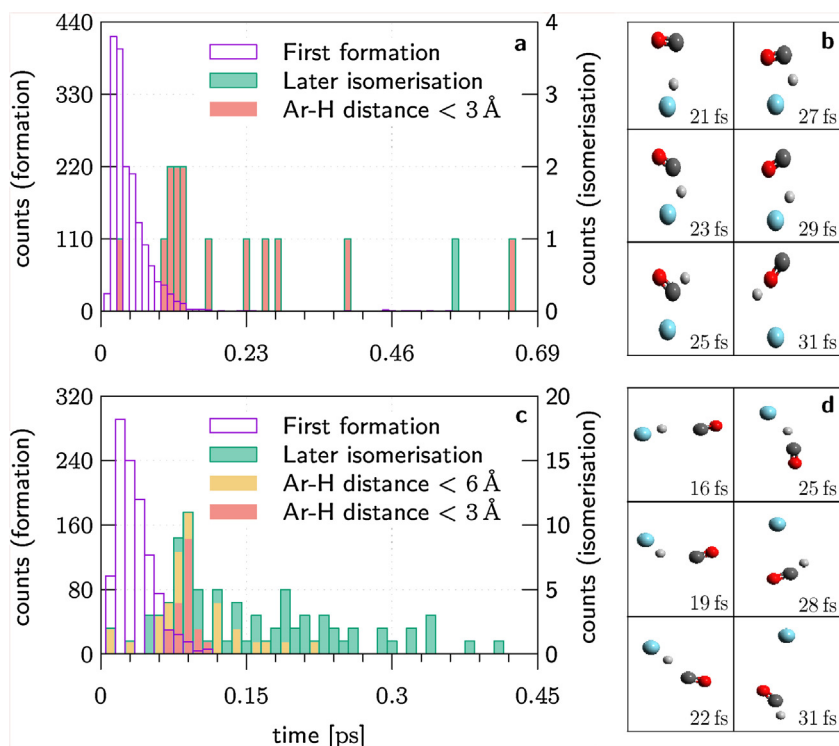
Fig. 10. Product formation times relative to the moment of nearest approach of the reactants ArH$^+$ and CO at (a) 0.83 eV and (c) 2.37 eV collision energy. Different scales are used for the counts of first product formation (left axis) and subsequent isomerisation events (right axis). Different colors show if the argon atom is near to the hydrogen atom during isomerisation. Example cartoons are shown for (b) an argon catalysed isomerisation with backward scattering at 0.83 eV and (d) a direct reaction with forward scattering at 2.37 eV.

parameters are more frequent, the large impact parameter range is an important contribution to the total HCO$^+$/HOC$^+$ branching close to 2:1 (see Table 1).

The region of small impact parameters is directly connected to products scattered backwards into large angles as depicted in Fig. 6c and d. The scattering angles decrease with increasing impact parameter to its minimum at the glory impact parameter and then rise due to the long-range attractive part [44] of the potential until the opacity function becomes zero. In case hydrogen approaches the C side of CO in a reaction towards HCO$^+$, the carbon monoxide is exposed to the deeper potential well such that the kinetic energy will be larger in the proximity to argon. This is related to a glory impact parameter that is on average slightly larger for HCO$^+$ than for HOC$^+$, as seen in Fig. 6c and d.

Related to the scattering angle, we note one peculiarity in the opacity function at the lower collision energy in Fig. 6a. With vanishing angle deflection near the respective glory impact parameter, the reaction probability for both HCO$^+$ and HOC$^+$ is enhanced at the lower collision energy. This leads to a maximum opacity of about 70% near $b = 3.4$ Å. This is not the case at the higher collision energy with less time for reorientation of the proton towards CO. Due to the higher energy, the transferred proton also bounces back to argon in 3 of a total of 11 non reactive trajectories near $b = 3.3$ Å.

In order to identify if isomerisation from HOC$^+$ to HCO$^+$ contributes to the computed preference for HCO$^+$ formation, we counted the number of initially formed and final products in different impact parameter ranges. HCO$^+$ molecules are detected in the trajectories when (i) the H–O distance is at least 1.2 times larger than the H–C distance, (ii) the sum of both distances is smaller than 5 Å and (iii) the bending angle relative to the linear geometry of the molecule is smaller than 70°. Condition (i) is inverted for detection of HOC$^+$. Only about 0.5% of the reactive trajectories undergo isomerisation after the initial product formation at impact parameters above 2 Å and we restrict the following discussion to $b < 2$ Å.

At 0.83 eV collision energy, isomerisation occurs in 3% of the reactions with $b < 2$ Å, but equally in both directions. The internal energy of the final products ranges from 2.4 to 3.2 eV (mean 2.8 ± 0.3 eV) and all isomerisation events below the autoisomerisation threshold of 3.1 eV (see Fig. 1) are catalysed by the argon atom. In contrast, isomerisation occurs in 13% of the reactions at 2.37 eV with $b < 2$ Å such that the initial HCO$^+$ branching of 61% is increased to 65%. This is due to isomerisation events in the presence of argon that occur at all internal energies and lead to HCO$^+$ formation in 14 of 16 cases. We note, however, that almost all isomerising trajectories come along with final internal energies starting near the autoisomerisation threshold (mean and spread 3.9 ± 0.5 eV), and the two isomers can no longer be distinguished.

Using the criteria for product formation that were described for the isomerisation statistics above, we can also deduce the times of initial product formation and later isomerisation in all trajectories. The formation times relative to the moment of the nearest approach of the reactants are presented in Fig. 10. The proton transfer typically occurs less than 0.1 ps after the nearest approach and is faster at the higher collision energy in Fig. 10c. A cartoon of a fast direct reaction with large impact parameter is presented in Fig. 10d. On average, at 0.83 and 2.37 eV, HCO$^+$ is formed after 4.2 ± 4.0 and 3.3 ± 1.9 ps after the nearest approach while HOC$^+$ as initially formed product requires 5.6 ± 4.4 and 3.9 ± 1.8 ps. The reaction times increase only slightly with the impact parameter in the order of 0.3 to 0.6 ps except at 0.83 eV where the mean time of HOC$^+$ formation increases to 7.7 ± 3.7 ps for $b > 4$ Å.

The few argon catalysed isomerisation events at the low collision energy, Fig. 10a, happen typically just after 0.1 ps but also at earlier times and up to more than 6 ps later. An example at early times is given by the cartoon in Fig. 10b. At 2.37 eV in Fig. 10c, no argon catalysed isomerisation was observed after 0.12 ps but later autoisomerisation may occur at all times as energy allows.
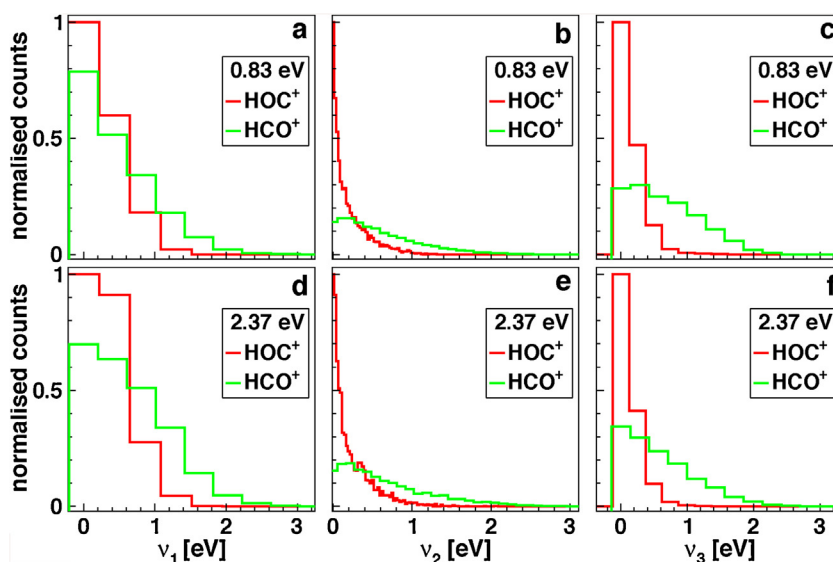
Fig. 11. Vibrational energy distributions from the normal mode analysis for the HO or HC stretching (ν_1), bending (ν_2) and CO stretching (ν_3) at (a)–(c) 0.83 eV and (d)–(f) 2.37 eV collision energy. The distributions for the HOC$^+$ and HCO$^+$ products are normalised to identical areas in each subplot. The bin widths are given by the vibrational energy quanta in harmonic approximation.

Table 3
Mean vibrational energies in eV from the normal mode analysis for the HC or HO stretching (ν_1), bending (ν_2) and CO stretching (ν_3). In brackets, the standard deviations of the distributions are given in units of the last digit. The total energy is compared to the experimental mean internal energy relative to the HCO$^+$ and HOC$^+$ ground state energy, respectively. Finally, the ratios between the higher and lower collision energy values are given.

Energy	Product	ν_1	ν_2	ν_3	E_{rot}	Total	Exp.
0.83 eV	HCO$^+$	0.4(5)	0.6(5)	0.6(5)	0.7(5)	2.3(4)	2.4(4)
		19%	24%	28%	29%	100%	
	HOC$^+$	0.2(3)	0.2(2)	0.1(2)	0.3(2)	0.8(3)	0.7(4)
		29%	23%	14%	35%	100%	
2.37 eV	HCO$^+$	0.6(6)	0.6(6)	0.6(5)	0.8(6)	2.6(6)	2.6(6)
		23%	25%	22%	30%	100%	
	HOC$^+$	0.3(3)	0.2(3)	0.1(2)	0.5(4)	1.1(5)	1.0(6)
		28%	20%	9%	41%	100%	
Ratio	HCO$^+$	1.35	1.14	0.88	1.17	1.12	1.10
Ratio	HOC$^+$	1.32	1.15	0.88	1.63	1.32	1.31

To locate the internal energy of the products, we performed a mode-specific vibrational analysis as described in Section 2.2. Both isomers feature two stretching (ν_1, ν_3) and a bending (ν_2) mode. The vibrational frequencies ω_1, ω_2, ω_3, at the PBE0 level with the 6-31G(d,p) basis set are 3261, 869 and 2294 cm^{-1} for HCO$^+$ and 3489, 201 and 1998 cm^{-1} for HOC$^+$. The non-integer harmonic actions are binned to integer values and presented with their corresponding energy scales in Fig. 11. The mean rotational and mode-specific vibrational energies with percentages are tabulated in Table 3 alongside the experimental mean internal energy.

The most striking difference between the isomers is the strongly increased excitation of the CO stretch (ν_3) in the HCO$^+$ products in Fig. 11c and f. Its mean fraction of the total internal excitation energy is about twice as large as for the HOC$^+$ products. Furthermore, it stands out because its population is not enhanced by the larger collision energy. We infer that the CO stretch excitation, the only mode that is only indirectly coupled to the reaction coordinate, is governed by the reaction enthalpy. It is assumed to be determined by the gain of potential energy due to the changed C–O equilibrium distance.

The vibrational energies in the HCO$^+$ products account for 70% of the total internal excitation and are almost equally distributed to all three modes at 2.37 eV collision energy. Most of the additional 0.3 eV internal energy at the larger collision energy is channelled

into the HC stretch mode (ν_1). This is also true in relative terms given by the enhancement ratios in Table 3. They are very similar for both isomers (comparing the HC to the HO stretch) except for the prominent increase by a factor 1.63 of the rotational excitation of HOC$^+$, that is generally more important for this isomer with a percentage of 35–41% as opposed to 30% for HCO$^+$.

The total mean internal energy agrees with the experimental results up to 0.1 eV. Despite the simulated exothermicity of 0.89 eV as opposed to 0.59 eV as calculated from literature values, it is only slightly overestimated for HOC$^+$.

4. Conclusion

The proton transfer reaction from ArH$^+$ to CO with the isomeric products HCO$^+$ and HOC$^+$ at collision energies ranging from 0.4 to 2.4 eV has been investigated experimentally using crossed beam imaging and theoretically with direct dynamics simulations. The reaction is characterised by a fast direct mechanism with little transfer between kinetic energy and internal excitation. Upon increasing the collision energy from 0.4 to 2.4 eV, the mean internal energy relative to the HCO$^+$ ground state increases from 2.2 to only 2.6 eV staying close to the exothermicity of 2.33 eV. The angle-differential analysis of the experimental data reveals that energy transfer from the collision energy to internal excitation on average only takes place at large scattering angles.

The small influence of the different exothermicities of the HCO$^+$ isomers on the product internal energy, or equivalently on the relative energy after the collision that is directly accessible in the experiments, makes it impossible to find an indicator to separate the isomeric products from the measured cross sections alone. This is in contrast to the HOCO$^+$ + CO reaction for which the HOC$^+$ product channel is endothermic, and the assumption of identical internal energy fractions of the total available energy for both isomers allowed the estimation of an upper limit of <2% for the HOC$^+$ fraction [27]. The present study suggests, that similar estimates for the H$_3^+$ + CO reaction [14] may have resulted in too small limits for the HOC$^+$ fraction which is supported by recent direct dynamics simulations [43].

The computed rate constant close to 1.3×10^{-9} cm^3 s^{-1} at both collision energies agrees well with the measured value of $1.25(35) \times 10^{-9}$ cm^3 s^{-1} from drift tube experiments [25]. The

simulations also show good agreement with the experimental distributions of the product internal energy and scattering angles. The simulated branching ratio of the isomeric products HCO$^+$ and HOC$^+$ is about 2:1 irrespective of the collision energy (0.83 eV and 2.37 eV). The branching is due to the larger opacity and maximum impact parameter for the thermodynamically favoured HCO$^+$ product. The product of a single reaction is strongly affected by the initial orientation of CO with respect to the relative velocity of the reactants.

The calculated opacity functions can be approximated by a constant of about 50% up to maximum impact parameters well beyond the simple capture limit. This gives rise to the dominant forward scattering that is also found in the experimental differential cross sections. At 0.83 eV collision energy, the reaction probability is enhanced to about 70% near the glory impact parameter. Apparently, at the impact parameter range of small angular deflection and little momentum transfer, there is enough time for ArH$^+$ to reorient the proton towards CO, and if so, the proton transfer almost always takes place—in contrast to higher collision energies where the proton is bouncing back to argon in several trajectories.

The simulated opacity function of HOC$^+$ formation is smaller than that for HCO$^+$ formation at all impact parameters and the maximum impact parameter for HOC$^+$ is almost 1 Å smaller than for HCO$^+$. At large impact parameters above the maximum for HOC$^+$ formation, the attractive force of the C side towards the proton may still be sufficient for the formation of HCO$^+$. This is also supported by the increase of the HOC$^+$ formation time relative to the time of nearest approach of the reactants for impact parameters larger 4 Å at 0.83 eV collision energy. The larger impact parameter range for the HCO$^+$ formation is an important contribution to the 2:1 branching ratio of the HCO$^+$ and HOC$^+$ products.

Isomerisation of the initially formed product to the other isomer was found to play a minor role for the product branching ratio. At 0.83 eV collision energy close to the threshold for autoisomerisation, argon catalyzed isomerisation takes place in 3% of all reactions, equally in both directions. Nearly all of the isomerising trajectories at 2.37 eV collision energy lead to products with internal energies above the autoisomerisation threshold so the products are indistinguishable. Due to this, the HCO$^+$ branching for impact parameters below 2 Å is increased from 61 to 65% due to isomerisation events in the presence of argon.

The mode-specific vibrational analysis of the products showed that the average CO stretch excitation is mostly independent of the collision energy and is energy wise about twice as large for HCO$^+$ than for HOC$^+$. We infer that it is largely determined by the reaction enthalpy. The mode specific relative enhancement of vibrational excitation by collision energy is not isomer specific and larger for the HC and HO stretch than for the bending mode. Rotational excitation accounts for 29–41% of the total internal excitation. It is more important for the HOC$^+$ isomer and noticeably increased by 63% from 0.83 to 2.37 eV collision energy, and by only 17% in the case of HCO$^+$.

Acknowledgements

References

[1] S. Petrie, D.K. Bohme, Ions in space, Mass Spectrom. Rev. 26 (2) (2006) 258–280, http://dx.doi.org/10.1002/mas.20114.

[2] D. Smith, The ion chemistry of interstellar clouds, Chem. Rev. 92 (1992) 1473–1485.

[3] B.J. McCall, Spectroscopy of trihydrogen(+) in laboratory and astrophysical plasmas, Department of Chemistry and Department of Astronomy and Astrophysics, University of Chicago, Chicago, IL, 2001, Ph.D. thesis.

[4] M. Larsson, H$_3^+$: the initiator of interstellar chemistry, Int. J. Astrobiol. 7 (3–4) (2008) 237–241, http://dx.doi.org/10.1017/S1473550408004230.

[5] E. Herbst, The astrochemistry of H$_3^+$, Philos. Trans. R. Soc. Lond. A: Math. Phys. Eng. Sci. 358 (1774) (2000) 2523–2534, http://dx.doi.org/10.1098/rsta.2000.0665.

[6] R.C. Woods, C.S. Gudeman, R.L. Dickman, P.F. Goldsmith, G.R. Huguenin, W.M. Irvine, A. Hjalmarson, L.-A. Nyman, H. Olofsson, The HCO$^+$/HOC$^+$ abundance ratio in molecular clouds, Astrophys. J. 270 (1983) 583–588, http://dx.doi.org/10.1086/161150.

[7] A.J. Apponi, T.C. Pesch, L.M. Ziurys, Detection of HOC$^+$ toward the Orion Bar and M17-SW: enhanced abundances in photon-dominated regions? ApJL 519 (1) (1999) L89, http://dx.doi.org/10.1086/312096.

[8] T. Amano, T. Nakanaga, Laboratory measurements of the abundance ratio HCO$^+$/HOC$^+$ and their astrophysical implications, Astrophys. J. 328 (1988) 373–379, http://dx.doi.org/10.1086/166299.

[9] E. Herbst, D.E. Woon, Why HOC$^+$ is detectable in interstellar clouds: the rate of the reaction between HOC$^+$ and H$_2$, ApJL 463 (2) (1996) L113.

[10] H. Liszt, R. Lucas, J.H. Black, The abundance of HOC$^+$ in diffuse clouds, A&A 428 (1) (2004) 117–120, http://dx.doi.org/10.1051/0004-6361:20041649.

[11] M. Mladenović, Theoretical spectroscopic parameters for isotopic variants of HCO$^+$ and HOC$^+$, J. Chem. Phys. 147 (11) (2017) 114111, http://dx.doi.org/10.1063/1.4998467.

[12] C. Savage, L.M. Ziurys, Ion chemistry in photon-dominated regions: examining the [HCO$^+$]/[HOC$^+$]/[CO$^+$] chemical network, Astrophys. J. 616 (2) (2004) 966, http://dx.doi.org/10.1086/424964.

[13] M.A. Smith, S. Schlemmer, J. von Richthofen, D. Gerlich, HOC$^+$ + H$_2$ isomerization rate at 25 K: implications for the observed [HCO$^+$]/[HOC$^+$] ratios in the interstellar medium, ApJL 578 (1) (2002) L87.

[14] E. Carrascosa, M.A. Kainz, M. Stei, R. Wester, Preferential isomer formation observed in H$_3^+$ + CO by crossed beam imaging, J. Phys. Chem. Lett. 7 (14) (2016) 2742–2747, http://dx.doi.org/10.1021/acs.jpclett.6b01028.

[15] M.J. Barlow, B.M. Swinyard, P.J. Owen, J. Cernicharo, H.L. Gomez, R.J. Ivison, O. Krause, T.L. Lim, M. Matsuura, S. Miller, G. Olofsson, E.T. Polehampton, Detection of a noble gas molecular ion, ^{36}ArH$^+$, in the crab nebula, Science 342 (6164) (2013) 1343–1345, http://dx.doi.org/10.1126/science.1243582.

[16] P. Schilke, D.A. Neufeld, H.S.P. Müller, C. Comito, E.A. Bergin, D.C. Lis, M. Gerin, J.H. Black, M. Wolfire, N. Indriolo, J.C. Pearson, K.M. Menten, B. Winkel, A. Sánchez-Monge, T. Möller, B. Godard, E. Falgarone, Ubiquitous argonium (ArH$^+$) in the diffuse interstellar medium: a molecular tracer of almost purely atomic gas, Astron. Astrophys. 566 (2014) A29, http://dx.doi.org/10.1051/0004-6361/201423727.

[17] H.S.P. Müller, S. Muller, P. Schilke, E.A. Bergin, J.H. Black, M. Gerin, D.C. Lis, D.A. Neufeld, S. Suri, Detection of extragalactic argonium, ArH$^+$, toward PKS 1830-211, Astron. Astrophys. 582 (2015) L4, http://dx.doi.org/10.1051/0004-6361/201527254.

[18] M. Majd, W. Paul, M. Michael, The composition of Mars' topside ionosphere: effects of hydrogen, J. Geophys. Res. [Space Phys.] 118 (5) (2014) 2681–2693, http://dx.doi.org/10.1002/jgra.50104.

[19] J.L. Fox, The chemistry of protonated species in the Martian ionosphere, Icarus 252 (2015) 366–392, http://dx.doi.org/10.1016/j.icarus.2015.01.010.

[20] P.J. Linstrom, in: W.G. Mallard (Ed.), NIST Chemistry WebBook, NIST Standard Reference Database Number 69, National Institute of Standards and Technology, Gaithersburg, MD, 2005 (retrieved 19.06.18).

[21] E.P.L. Hunter, S.G. Lias, Evaluated gas phase basicities and proton affinities of molecules: an update, J. Phys. Chem. Ref. Data 27 (3) (1998) 413–656, http://dx.doi.org/10.1063/1.556018.

[22] J.C. Traeger, Heat of formation for the formyl cation by photoionization mass spectrometry, Int. J. Mass Spectrom. Ion Process. 66 (3) (1985) 271–282, http://dx.doi.org/10.1016/0168-1176(85)80002-1.

[23] Report of the ICSU-CODATA task group on key values for thermodynamics, November, 1971, J. Chem. Thermodyn. 4 (3) (1972) 331–336, http://dx.doi.org/10.1016/0021-9614(72)90016-X.

[24] C.G. Freeman, J.S. Knight, J.G. Love, M.J. McEwan, The reactivity of HOC$^+$ and the proton affinity of CO at O, Int. J. Mass Spectrom. Ion Process. 80 (1987) 255–271, http://dx.doi.org/10.1016/0168-1176(87)87034-9.

[25] H. Villinger, J.H. Futrell, F. Howorka, N. Duric, W. Lindinger, The proton transfer from ArH$^+$ to various neutrals, J. Chem. Phys. 76 (7) (1982) 3529–3534, http://dx.doi.org/10.1063/1.443454.

[26] R.E. Rosati, M.P. Skrzypkowski, R. Johnsen, M.F. Golde, Yield of excited CO molecules from dissociative recombination of HCO$^+$ and HOC$^+$ ions with electrons, J. Chem. Phys. 126 (15) (2007) 154302, http://dx.doi.org/10.1063/1.2715943.

[27] E. Carrascosa, M. Stei, M.A. Kainz, R. Wester, Isomer-specific product formation in the proton transfer reaction of HOCO$^+$ with CO, Mol. Phys. 113 (24) (2015) 3955–3963, http://dx.doi.org/10.1080/00268976.2015.1075620.

[28] R. Wester, Velocity map imaging of ion-molecule reactions, Phys. Chem. Chem. Phys. 16 (2014) 396–405, http://dx.doi.org/10.1039/C3CP53405G.

[29] R. Otto, J. Brox, S. Trippel, M. Stei, T. Best, R. Wester, Single solvent molecules can affect the dynamics of substitution reactions, Nat. Chem. 4 (7) (2012) 534–538, http://dx.doi.org/10.1038/NCHEM.1362.

[30] C. Rebrion, B.R. Rowe, J.B. Marquette, Reactions of Ar^+ with H_2, N_2, O_2, and CO at 20, 30, and 70 K, J. Chem. Phys. 91 (10) (1989) 6142–6147, http://dx.doi.org/10.1063/1.457433.

[31] A.T.J.B. Eppink, D.H. Parker, Velocity map imaging of ions and electrons using electrostatic lenses: application in photoelectron and photofragment ion imaging of molecular oxygen, Rev. Sci. Instrum. 68 (9) (1997) 3477–3484, http://dx.doi.org/10.1063/1.1148310.

[32] S. Trippel, M. Stei, R. Otto, P. Hlavenka, J. Mikosch, C. Eichhorn, A. Lourderaj, J. Zhang, W.L. Hase, M. Weidemüller, R. Wester, Kinematically complete chemical reaction dynamics, J. Phys.: Conf. Ser. (ICPEAC 2009) 194 (2009) 012046, http://dx.doi.org/10.1088/1742-6596/194/1/012046.

[33] X. Hu, W.L. Hase, T. Pirraglia, Vectorization of the general Monte Carlo classical trajectory program VENUS, J. Comput. Chem. 12 (8) (1991) 1014–1024, http://dx.doi.org/10.1002/jcc.540120814.

[34] M. Valiev, E.J. Bylaska, N. Govind, K. Kowalski, T.P. Straatsma, H.J.J.V. Dam, D. Wang, J. Nieplocha, E. Apra, T.L. Windus, W.A. de Jong, NWChem: a comprehensive and scalable open-source solution for large scale molecular simulations, Comput. Phys. Commun. 181 (9) (2010) 1477–1489, http://dx.doi.org/10.1016/j.cpc.2010.04.018.

[35] U. Lourderaj, R. Sun, S.C. Kohale, G.L. Barnes, W.A. de Jong, T.L. Windus, W.L. Hase, The VENUS/NWChem software package. Tight coupling between chemical dynamics simulations and electronic structure theory, Comput. Phys. Commun. 185 (3) (2014) 1074–1080, http://dx.doi.org/10.1016/j.cpc.2013.11.011.

[36] C. Adamo, V. Barone, Toward reliable density functional methods without adjustable parameters: the PBE0 model, J. Chem. Phys. 110 (13) (1999) 6158–6170, http://dx.doi.org/10.1063/1.478522.

[37] R. Ditchfield, W.J. Hehre, J.A. Pople, Self-consistent molecular-orbital methods. IX. An extended Gaussian-type basis for molecular-orbital studies of organic molecules, J. Chem. Phys. 54 (2) (1971) 724–728, http://dx.doi.org/10.1063/1.1674902.

[38] C. Eckart, Some studies concerning rotating axes and polyatomic molecules, Phys. Rev. 47 (1935) 552–558, http://dx.doi.org/10.1103/PhysRev.47.552.

[39] A.Y. Dymarsky, K.N. Kudin, Computation of the pseudorotation matrix to satisfy the Eckart axis conditions, J. Chem. Phys. 122 (12) (2005) 124103, http://dx.doi.org/10.1063/1.1864872.

[40] G. Czakó, Gaussian binning of the vibrational distributions for the $Cl + CH_4$ ($v_{4/2}$=0.1) → $H + CH_3Cl(n_1 n_2 n_3 n_4 n_5 n_6)$ reactions, J. Phys. Chem. A 116 (28) (2012) 7467–7473, http://dx.doi.org/10.1021/jp3044797.

[41] Y. Zhu, L. Ping, M. Bai, Y. Liu, H. Song, J. Li, M. Yang, Tracking the energy flow in the hydrogen exchange reaction $OH + H_2O \rightarrow H_2O + OH$, Phys. Chem. Chem. Phys. 20 (2018) 12543–12556, http://dx.doi.org/10.1039/C8CP00938D.

[42] G.H.F. Diercksen, B.O. Roos, A.J. Sadlej, Legitimate calculation of first-order molecular properties in the case of limited CI functions. Dipole moments, Chem. Phys. 59 (1) (1981) 29–39, http://dx.doi.org/10.1016/0301-0104(81)80082-1.

[43] E.G. Naz, S. Godara, M. Paranjothy, Direct chemical dynamics simulations of H_3^+ + CO bimolecular reaction, J. Phys. Chem. A 122 (43) (2018) 8497–8504, http://dx.doi.org/10.1021/acs.jpca.8b08671.

[44] R.D. Levine, Molecular Reaction Dynamics, Cambridge University Press, 2009.